PHYSICAL REVIEW B **103**, 134432 (2021)

Crystallographic direction related spin current transmission in MgO(001)/$Fe_{0.79}Si_{0.21}$(001)/Pt(111) epitaxial bilayers

Jian Mao, Zhi Heng Yao, Xu Zhang, Jijun Yun, Meixia Chang, Yalu Zuo, and Li Xi*

Key Laboratory for Magnetism and Magnetic Materials of Ministry of Education,
Lanzhou University, Lanzhou, 730000, People's Republic of China

(Received 26 August 2020; revised 7 April 2021; accepted 12 April 2021; published 22 April 2021)

Spin-pumping and spin-orbit torque efficiencies in ferromagnetic/heavy metal bilayers, which usually consist of the polycrystalline grains, are related to the spin current transmission from ferromagnets to heavy metals and vice versa, respectively. In this work, epitaxial $Fe_{0.79}Si_{0.21}$(001)/Pt(111) films were fabricated to investigate the spin-pumping efficiency and spin-orbit torque efficiency by ferromagnetic resonance and harmonic Hall resistance measurement techniques, respectively. Ferromagnetic resonance results show that the incremental magnetic damping constants in epitaxial $Fe_{0.79}Si_{0.21}$(001)/Pt(111), compared with those of the epitaxial $Fe_{0.79}Si_{0.21}$(001)/AlO_x reference sample, depend on whether the external magnetic field is applied along the in-plane easy or hard axes of $Fe_{0.79}Si_{0.21}$. The Pt thickness-dependent anisotropic damping constant was ascribed to the anisotropic spin current absorption in epitaxial Pt(111) layer. When electric currents were applied along the easy and hard axes of $Fe_{0.79}Si_{0.21}$ in epitaxial $Fe_{0.79}Si_{0.21}$(001)/Pt(111) bilayers, a large difference between spin-orbit torques generated from Pt(111) was observed by a harmonic Hall resistance measurement method. Both of the results suggest that spin current transmission efficiency is related to the anisotropic spin Hall effect of epitaxial Pt(111) layer due to the different spin-orbit interaction energies along the different crystallographic directions of Pt.

DOI: 10.1103/PhysRevB.103.134432

I. INTRODUCTION

Spin current transmissions through the interface of ferromagnetic/heavy metal (FM/HM) bilayers could alert spin-dependent effect, such as spin-pumping and spin-orbit torque (SOT) effects. These effects play a crucial role in applications including racetrack memories [1], SOT-based magnetic random access memories [2], and other spintronic devices [3,4], due to their significant influence on the energy dissipation and information writing speed in magnetic memories [5]. The spin-pumping effect refers to the precession of the magnetic moment of ferromagnetic layer to transfer its excess angular momentum to the adjacent heavy metal layer via transferring spin current across the interface from FM to HM in FM/HM bilayer system [6]. When the spin current is absorbed by HM layer, it generates a dampinglike torque acting on the FM layer and gives rise to an additional damping constant (Δa) of FM except for its original damping constant (α) [7]. The magnetic damping constant α refers to the parameter in damping term $\alpha\hat{m} \times \frac{d\hat{m}}{dt}$, where $\hat{m}$ represents the unit vector of magnetization **M.** This damping term describes the viscous resistance during the precession of the magnetization in the phenomenological Landau-Lifshitz-Gilbert equation [8]. The damping constant of FM/HM can be obtained from the ferromagnetic resonance (FMR) measurement through the analysis of the frequency-dependent FMR linewidth [9]. Using this method, the spin-pumping efficiency, i.e., the spin current injection efficiency of FM/HM bilayers, can be characterized by the increased damping constant Δa [10]. Spin-orbit torque refers to the phenomenological torque induced by spin current generated in HM or spin accumulation in FM/HM interface through spin Hall effect [11] or Rashba effect [12] when applying an electric current in HM layers. The spin-orbit torque efficiency can be characterized by the harmonic Hall voltage measurement method for perpendicular magnetized FM/HM sample [13] and in-plane magnetized FM/HM sample [14].

In the past, except that many works have experimentally reported the variation of the damping constant and spin-mixing conductance in FM/HM bilayers with a polycrystalline phase of ferromagnetic thin films [9,15], more and more works paid attention to the influence of spin-pumping induced extra damping constant in the epitaxial FM layers. For example, Cahaya *et al.* [16] reported that the crystal fields in different crystallographic directions of $CoFe_2O_4$ samples can lead to the anisotropic spin current injection and absorption. Isasa *et al.* reported a different spin mixing conductance at (111) and (001) $CoFe_2O_4$/Pt interfaces [17]. Considering different crystal orientation of FM layer can induce anisotropic spin-pumping effect, it is natural to ask whether the HM layer with different crystallographic directions could also induce an anisotropic spin current absorption/generation in FM/HM heterostructures. Actually, a theoretical calculation indeed shows an anisotropic damping constant in Co/Pt and Co/Pd superlattices with (111), (001), and (011) orientations of Pt or Pd [18]. In addition, the anisotropic spin Hall effect in antiferromagnetic layer with different crystallographic directions has also been studied by Zhang *et al.* experimentally [19]. In this work,

---

*xili@lzu.edu.cn

the anisotropic spin Hall effect was investigated in a fully epitaxial $\mathrm{Fe_{0.79}Si_{0.21}(001)/Pt(111)}$ bilayer grown on MgO(001) single-crystal substrates. Here we choose Pt as the spin current absorption/generation layer due to its strong spin-orbit coupling strength [20–24] and the quite small lattice mismatch with MgO and $\mathrm{Fe_{0.79}Si_{0.21}}$ alloys [25,26]. Ferromagnetic resonance (FMR) technology was used to explore the phenomenon related to the spin pumping and the enhancement of magnetic damping constant in the epitaxial FeSi(001)/Pt(111) bilayers with the applied external magnetic field along the in-plane easy or hard axes of $\mathrm{Fe_{0.79}Si_{0.21}}$. Harmonic Hall voltage measurements on $\mathrm{MgO(001)/Fe_{0.79}Si_{0.21}(001)/Pt(111)}$ were conducted to acquire the spin-orbit torque efficiency with electric current along different crystallographic directions of $\mathrm{Fe_{0.79}Si_{0.21}(001)}$. The obtained results confirm the anisotropic spin Hall effect in epitaxial Pt(111).

II. EXPERIMENT

$\mathrm{Fe_{0.79}Si_{0.21}(001)/Pt}$ and a reference sample of $\mathrm{Fe_{0.79}Si_{0.21}(001)/AlO_{\mathit{x}}}$ in films were fabricated on $10 \times 10\text{-mm}^2$ sized MgO(001) single-crystalline substrates by radio frequency magnetron sputtering with the base pressure lower than 4.5×10^{-5} Pa and the processing gas of Ar around 0.5 Pa. The deposition powers are 120 and 10 W for 3-in Fe target with Si chips mounted on Fe surface and 2-in Pt target, respectively. To weaken the contribution of damping constant from two magnon scattering, a relative large nominal thickness around 10 nm for $\mathrm{Fe_{0.79}Si_{0.21}}$ was chosen [27,28], while the nominal thicknesses of Pt(t_{Pt}) are varying from 1.5 to 7.0 nm to investigate the thickness-dependent spin current absorption properties and 1.0-nm-thick Al layer was deposited to avoid oxidation of $\mathrm{Fe_{0.79}Si_{0.21}}$. Substrates were heat treated at 873 K for 1 h to remove the contamination of the substrate prior to film growth. During deposition of $\mathrm{Fe_{0.79}Si_{0.21}}$ films, substrate temperature was kept at 873 K, while Pt(111) and Pt(001) films were deposited with substrate temperature around 300 and 673 K, respectively.

The high-resolution x-ray-diffraction (XRD) patterns of thin films were collected by a PANalytical X′Pert^3 diffractometer using CuK$_a$ ($\lambda = 0.154\ 06\,\mathrm{nm}$) radiation. The composition of $\mathrm{Fe_{0.79}Si_{0.21}}$(FeSi) was measured by the energy-dispersive x-ray spectroscopy. The high-resolution cross-sectional image of MgO/FeSi/Pt sample was taken by transmission electron microscopy (TEM). The cross-sectional TEM sample was prepared by focused ion-beam technique and further polished to remove the surface amorphous layers by argon ion-beam milling system prior to transfer the sample to TEM. The magnetic hysteresis loops and the angular-dependent remanent magnetization curves were measured by a MicroSense EV9 vibrating sample magnetometer (VSM) [26] with the magnetic field resolution and sweep rates around 0.1 and 1 Oe per second, respectively. The actual thickness and interface/surface roughness of each layer were determined by simulating the specular x-ray reflectivity (XRR) spectra using the GEN’X reflectivity-fitting package [29,30]. The frequency dependent FMR spectra were recorded by a broadband Nanos Instrument Phaser system [31] in the frequency (f) range from 2 to 18 GHz with external magnetic field (H_{ext}) along the easy or hard axes of FeSi. The in-plane magnetic field-dependent FMR spectrum was measured using a JEOL JES-FA 300 electron spin resonance (ESR) spectrometer working at 9.0 GHz by scanning DC magnetic field in the range of 0–20 000 Oe. In this experiment the sample was fixed on a quartz rod and a goniometer was used to control the rotation angle in the film plane.

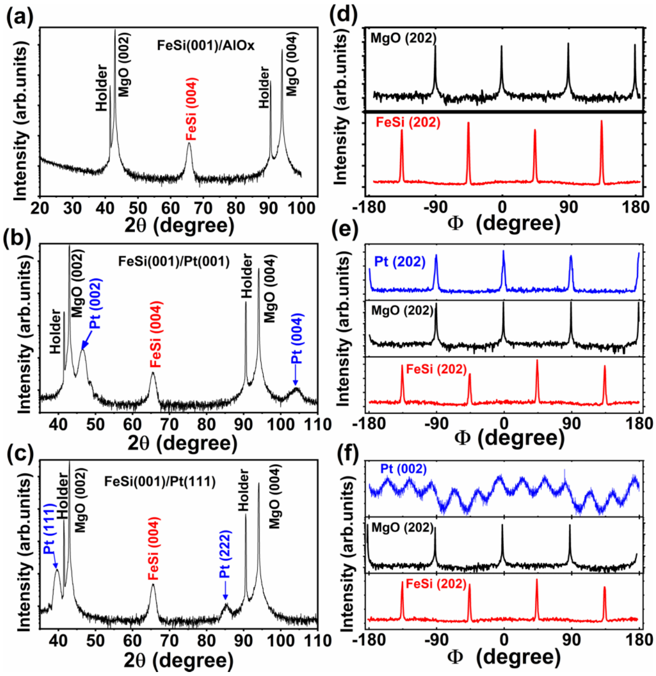

FIG. 1. High-resolution XRD patterns for samples grown on (001)MgO: $\mathrm{FeSi(001)/AlO_{\mathit{x}}}$ (a), FeSi(001)/Pt(001) (b), FeSi(001)/Pt(111) (c), and the Φ-scan patterns of FeSi(202), MgO(202), and Pt(202) lattice planes for $\mathrm{FeSi(001)/AlO_{\mathit{x}}}$ (d), FeSi(001)/Pt(001) (e), and Pt(002) lattice plane for FeSi(001)/Pt(111) (f).

The spin-orbit torque efficiency was measured in FeSi(001)/Pt(111) with Pt thickness (t_{Pt}) around 7 nm through harmonic Hall voltage measurement method to obtain the effective fields of dampinglike and fieldlike torques [14]. For this measurement, the films were patterned into 20-μm-wide Hall bars using standard photolithography and argon ion-milling techniques with the current channel parallel to either the in-plane easy axis or hard axis of FeSi(001) films. The first and second harmonic Hall voltage were measured by an Analog-Digital/Digital-Analog data acquisition card with a 133-Hz sinusoidal current along the x axis (i.e., the current channel of Hall bars); meanwhile, scanning fields $H_{y\text{-ext}}$ were applied along the in-plane y axis with a fixed external field $H_{x\text{-ext}}$ along the x axis. All the above experiments were performed at room temperature.

III. RESULTS AND DISCUSSION

The ω-2θ XRD patterns for FeSi/Pt films and the reference $\mathrm{FeSi/AlO_{\mathit{x}}}$ sample are presented in Fig. 1. In Figs. 1(a)–1(c), the strong peaks located at $2\theta = 42.98^\circ$ and 93.85° arise from (002) and (004) lattice plane of the single-crystal MgO(001) substrate, respectively. The peak at $2\theta = 65.71^\circ$ can be ascribed to the (004) lattice plane of FeSi. The lattice constants (a) for MgO(001) and FeSi(001) were calculated to be 0.421 and 0.568 nm using Bragg's law with $2\theta = 42.98^\circ$ and 65.71°, respectively. The lattice mismatch between FeSi and MgO substrate is around −4.6% using the formula of $(a_{\mathrm{FeSi}}/\sqrt{2}\text{-}a_{\mathrm{MgO}})/a_{\mathrm{MgO}}$. It should be noted that the additional quite sharp and narrow peaks located at $2\theta = 41.41^\circ$ and 90.57°, respectively, come from the (006) and (0012) planes of an $\mathrm{Al_2O_3}$ single-crystal sample holder in XRD measurements due to our small-sized samples. In order to confirm the epitaxial relationship between MgO and FeSi, the Φ scans for a specific lattice plane were measured. Figures 1(d) and 1(e) show the Φ-scan results of (202) lattice plane of MgO and FeSi, and the (202) lattice plane of Pt for FeSi/AlO$_x$ and FeSi/Pt(001), respectively. One can see two sets of fourfold symmetry diffraction peaks with the exact angle difference of 45° between them. It suggests the epitaxial relationship of MgO(001)[100]‖FeSi(001)[110], while for FeSi/Pt sample with Pt deposited at 673 K, it shows only two peaks located at $2\theta = 46.36^\circ, 104.32^\circ$, which correspond to the (002) and (004) lattice plane of Pt with face-centered cubic (fcc) structure. The Φ-scan pattern for (202) plane of Pt grown at 673 K shows another fourfold symmetry and has a 45° difference with respect to those of FeSi(202), indicating the epitaxial relationship among them: MgO(001)[100]‖FeSi(001)[101]‖Pt(001)[100]. For FeSi/Pt sample with Pt grown at substrate temperature $T_s = 300$ K, the XRD pattern shows two peaks at $2\theta = 39.72^\circ, 85.21^\circ$, which can be ascribed to the (111) and (222) lattice plane of fcc Pt. The Φ-scan pattern for (002) lattice plane of (111)-oriented Pt displays 12 reflections with 30° between two adjacent peaks were also found in our sample. It suggests an epitaxial relationship for Pt grown at 300 K with epitaxial relationship of MgO(001)[100]‖FeSi(001)[101]‖Pt(111)[110] [32]. The full epitaxial growth of Pt on FeSi(001) could be explained by the quite low lattice mismatch between Pt and FeSi with the calculated Pt lattice constant around 0.392 and 0.391 nm with $2\theta = 39.72^\circ$ and 46.36° for Pt grown at 300 and 673 K, respectively.

Figure 2 shows the x-ray reflectivity spectra and the depth profiles of the simulated x-ray scattering length density (SLD). For all samples, the distinct Kiessig fringes can be observed and well fitted. SLD profiles are plotted in Figs. 2(d)–2(f). Labels in the plots for each film stack give the simulated results for the thickness t, the interface/surface roughness σ, and the density ρ of each layer. The thickness of FeSi is approximately 10.43, 12.10, and 11.10 nm and the interface roughness σ between FeSi and the nonmagnetic layer are about 0.78, 0.36, and 0.62 nm for FeSi(001)/AlO$_x$, FeSi(001)/Pt(111), and FeSi(001)/Pt(001) films, respectively. The slightly increased value of σ in FeSi/Pt samples indicates the increase of interface diffusion between FeSi and Pt due to the higher substrate temperature for the formation of (001)-oriented Pt layers. Moreover, the higher substrate temperature may be also responsible for the increased density of FeSi from 5.53 to 6.31 g/cm^3 for (111) and (001) Pt-covered samples, respectively. However, the simulated density of Pt at different growth temperature is nearly the same with the magnitude around 20.0 g/cm^3. The relatively small roughness in all samples may suggest a high quality of our samples.

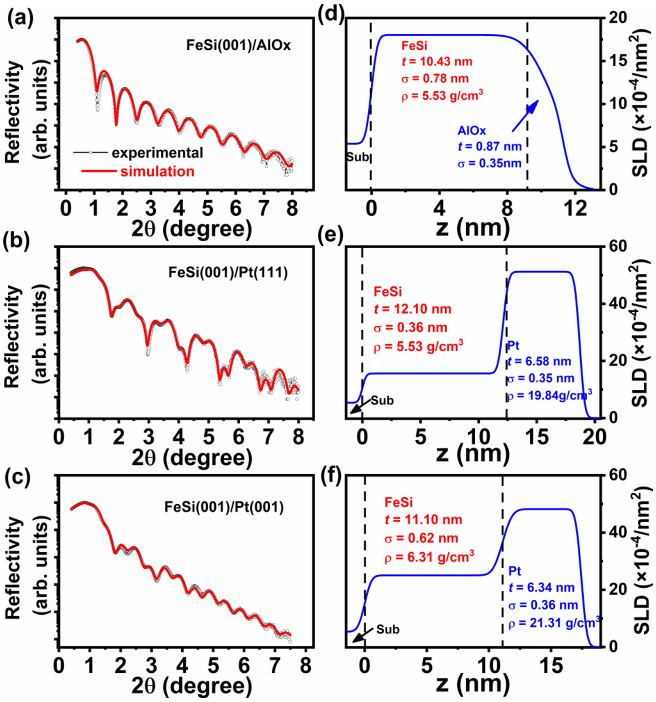

FIG. 2. X-ray reflectivity spectra of FeSi(001)/AlO$_x$ (a), FeSi(001)/Pt(111) (b), and FeSi(001)/Pt(001) (c) (black circles represents the experimental data and the red lines represent the fitting curves) and x-ray scattering-length density (SLD) vs depth profile for FeSi(001)/AlO$_x$ (d), FeSi(001)/Pt(111) (e), and FeSi(001)/Pt(001) (f) films. Labels in the map give the simulated parameters of the thickness (t), interface/surface roughness (σ), and density (ρ) of each layer.

TEM was used to get a clear and direct cross-sectional image of our epitaxial sample. Figure 3(a) shows the conventional cross-sectional TEM image of MgO(001)/FeSi(001)/Pt(111) sample with primary electron beam parallel to the [010] direction of the MgO substrate. The obtained thickness of FeSi and Pt are, respectively, around 11.5 and 6.9 nm, which are nearly consistent with XRR fitting results. Figure 3(b) shows the high-resolution TEM image of MgO/FeSi layers. It shows the nearly perfect arrangement of atoms in MgO substrate, FeSi layer, and even in their interface, indicating the high quality of single-crystal FeSi layer grown on the MgO(001) substrate with the quite small lattice mismatch. The left and right insets in Fig. 3(b), respectively, show the fast Fourier transformation plots from the MgO substrate and FeSi layer. The spots in the insets clearly exhibits the epitaxial relationship with MgO(001)[100]‖FeSi(001)[101]. Figure 3(c) shows the high-resolution TEM image of FeSi/Pt. The obtained distance between the vertical lattice planes of Pt is around 0.218 nm, which is quite close to the interplanar spacing of Pt(111). TEM images have confirmed the high quality of our epitaxial layer, which is complementary to the XRD and XRR data.

The hysteresis loops and angular-dependent remanent magnetization curves are shown in Figs. 4(a)–4(c). It shows a 90° repetition for the easy-axis (EA, $H\|\mathrm{MgO}\langle 110\rangle$) and hard-axis (HA, $H\|\mathrm{MgO}\langle 100\rangle$) loops together with the fourfold symmetry of the angular-dependent remanent

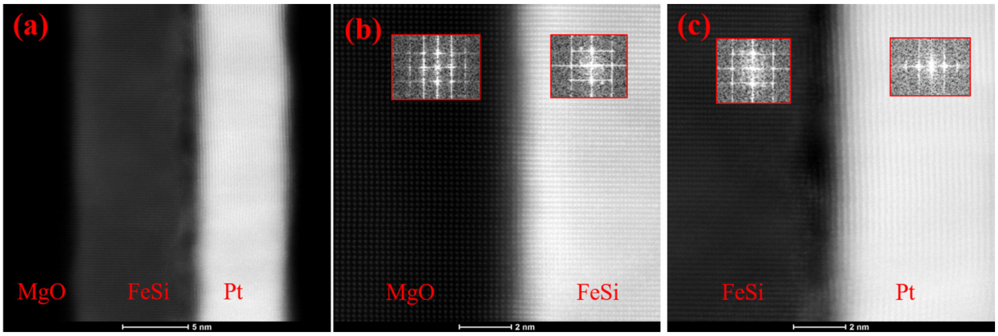

FIG. 3. Cross-sectional TEM image of MgO/FeSi/Pt sample (a), the high-resolution TEM image in MgO and FeSi layers (b), as well as in FeSi and Pt layers (c). The insets in (b) and (c) shows the fast Fourier transform plots of the corresponding layers.

magnetization curves for all samples. It indicates that FeSi has the cubic magnetocrystalline anisotropy [25,26]. The cubic magnetic anisotropy of FeSi is also confirmed by the in-plane angular-dependent FMR spectra as shown in Fig. 4(d), in which the fitting curves based on the equation of $H_\mathrm{r} = H_\mathrm{r}^{\mathrm{ave}} + H_\mathrm{K}^{\mathrm{C}}\cos(4\varphi)$ with $H_\mathrm{r}^{\mathrm{ave}}$ and $H_\mathrm{K}^{\mathrm{C}}$ the average resonance field and cubic magnetocrystalline anisotropy field [33], respectively. It should be noted that the angular-dependent resonance field for FeSi(001)/Pt(001) shows large difference with those curves for FeSi(001)/AlO$_x$ FeSi(001)/AlO$_x$, and FeSi(001)/Pt(111) samples. It may be ascribed to the large contribution from the strong interface alloying-induced variation of magnetic anisotropy due to the higher deposition temperature for FeSi(001)/Pt(001) sample. From the above static and dynamic magnetic properties measurement, the saturation magnetization ($4\pi M_\mathrm{S}$) are 14.02, 14.16, and 14.82 kG for FeSi(001)/AlO$_x$, FeSi(001)/Pt(111), and FeSi(001)/Pt(001) samples with $H_\mathrm{K}^{\mathrm{C}}$ around 123.2, 146.0, and 98.2 Oe, respectively. The magnetic properties of FeSi are consistent with the epitaxial structure of FeSi.

The FMR spectra of all samples were recorded up to the available maximum microwave frequency around 18 GHz. Figures 5(a) and 5(d) show the typical FMR spectra of FeSi(001)/Pt(111) sample with $t_{\mathrm{Pt}} = 7$ nm with H_{ext} along the MgO[110] or MgO[100], which correspond to the EA or HA of the FeSi films, respectively. The line-shape parameters, i.e.,

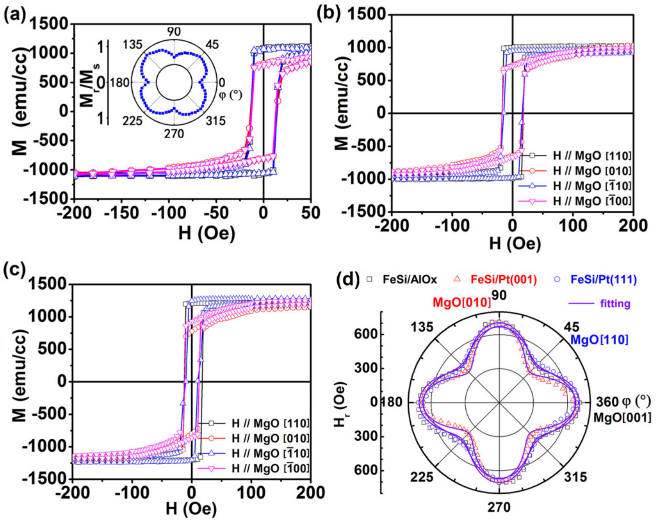

FIG. 4. Magnetic hysteresis loops of FeSi(001)/AlO$_x$ (a), FeSi(001)/Pt(111) (b), and FeSi(001)/Pt(001) (c) with magnetic field H applied parallel to the crystallographic axes of [110], [010], [$\bar{1}$10], and [$\bar{1}$00] of MgO. The in-plane angular dependence of resonance field H_r with respect to one of the substrate edges for three samples (d). The inset in (a) shows the exemplary angular-dependent remanence curves for FeSi(001)/AlO$_x$ sample.

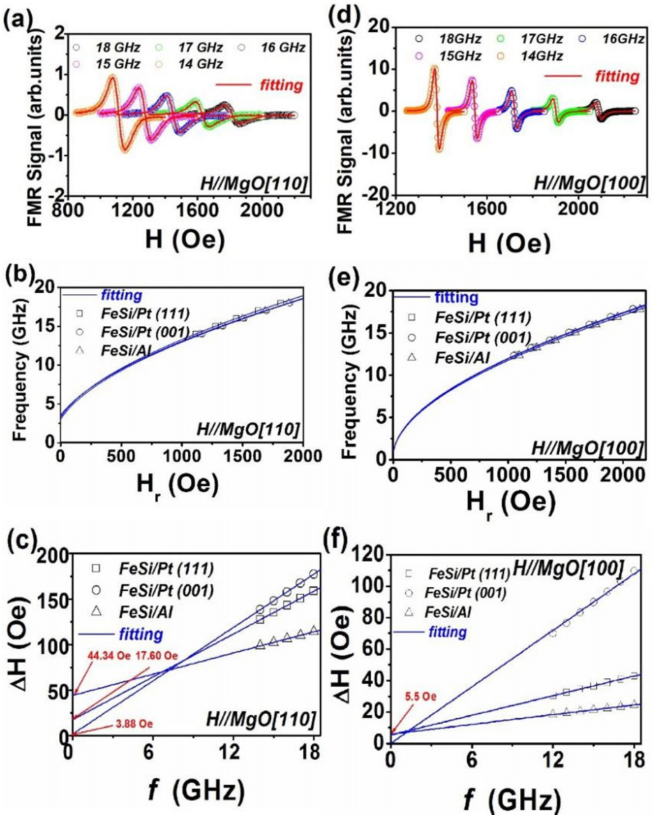

FIG. 5. Typical FMR spectra recorded at various frequencies for FeSi(001)/Pt(111) sample with external field applied along easy axis (MgO[110]) (a) and hard axis (MgO[100]) (d). (b) and (c) represent H_r vs f and ΔH vs f at easy axis for three samples, respectively. (e) and (f) represent H_r vs f and ΔH vs f at hard axis for three samples, respectively. The fitting curves in (b) and (e) are based on Eq. (1). The linear fitting curves in (c) and (f) are based on Eq. (2). Here the nominal thickness of Pt is 7 nm for FeSi(001)/Pt samples.

the resonance field (H_r) and the full width at half maximum linewidth (ΔH), were obtained by fitting the FMR spectra using the derivative of symmetric and antisymmetric Lorentzian functions [34,35].

When H_{ext} is applied along EA or HA of FeSi(001), the effective saturation magnetization ($4\pi M_{eff}$) and the cubic magnetocrystalline anisotropy constant (K_C) for an epitaxial thin film with cubic crystal structure can be extracted from Kittel's equation as [36]

$$f^2 = \left(\frac{\gamma}{2\pi}\right)^2 \left(H_r \mp \frac{2K_C}{4\pi M_S}\right) \times \left(H_r + 4\pi M_{eff} + \frac{2K_C}{4\pi M_S}\right), \tag{1}$$

where the sign of plus and minus correspond to H_{ext} along EA and HA respectively. γ is the gyromagnetic ratio and equals to $g\mu_B/\hbar$ with Landé g factor g around 2.08 for FeSi alloy [37], μ_B is the Bohr magneton, and $\hbar$ is the reduced Planck's constant. The effective saturation magnetization $4\pi M_{eff}$ ($=4\pi M_S$-$H_\perp$) were extracted by fitting the frequency dependence of resonance fields with Eq. (1). Here, $H_\perp$ represents the possible perpendicular magnetic anisotropy field. The frequency dependence of H_r was plotted in Figs. 5(b) and 5(e). The extracted $H_K{}^C (=2K_C/4\pi M_S)$ are around 118.3, 132.2, and 100.1 Oe, and $4\pi M_{eff}$ are about 13.4, 15.3, and 16.0 kG for FeSi(001)/AlO$_x$, FeSi(001)/Pt(111), and FeSi(001)/Pt(001) with $t_{Pt} = 7$ nm using Eq. (1), respectively. $H_K{}^C$ in all samples is comparable to those of the measured values by VSM and angular-dependent ESR. Generally, for a pure Gilbert-like viscous damping, ΔH dependence on the frequency can be described as [38,39]

$$\Delta H = \Delta H_0 + 4\pi\alpha f/\gamma, \tag{2}$$

where ΔH_0 describes the inhomogeneous resonance peak broadening and is related to the film quality. One can see that ΔH vs f curves all show quite linear response, indicating that the two-magnon scattering (TMS)-induced damping is negligibly small [36,40–42]. The negligible contribution of TMS may be ascribed to the quite large thickness of FeSi in this work [27,28]. The slopes of ΔH vs f curve show a quite large difference when H_{ext} is along the EA and HA as shown in Figs. 5(c) and 5(f). Moreover, the calculated effective damping constants α using Eq. (2) when H_{ext} along EA are larger than those with H_{ext} along HA for three samples. It should be noted that α with field along the EA is nearly 4 times larger than that with field along the HA for the epitaxial FeSi(001)/AlO$_x$ reference sample. Actually, the difference of α between different crystallographic directions is also observed in epitaxial Co$_2$MnSi and CoFe alloys [41,43,44]. The phenomena are ascribed to the different spin-orbit interaction energies along the different crystallographic directions [41,43]. So, the crystallographic directions-related spin-orbit interaction energies may also be responsible for the anisotropic damping constant along EA and HA in our epitaxial FeSi films.

Next, we focused on the spin-pumping induced extra damping constant Δa, which can be determined by the difference between damping constant of FeSi(001)/Pt sample and that of the FeSi(001)/AlO$_x$ reference sample. So, the increase in damping constant and the spin-mixing conductance of FeSi(001)/Pt were investigated in comparison with those of the reference FeSi/AlO$_x$ sample when the field was along different crystallographic directions. Comparing with the reference sample, an additional enhancement of damping constant Δa was observed when H_{ext} was applied along the EA and HA of FeSi films in both Pt(001) and Pt(111)-covered samples as shown in Fig. 6(c). When H_{ext} was applied along EA and HA of FeSi/Pt films with t_{Pt} around 7 nm, Δa is about 7.96×10^{-3} and 7.88×10^{-3} for FeSi(001)/Pt(001) sample, while it is about 3.68×10^{-3} and 1.40×10^{-3} for FeSi(001)/Pt(111) sample, respectively. The small difference of Δa between two crystalline directions for FeSi(001)/Pt(001) sample may be ascribed to two facts: the large interface intermixing between FeSi and Pt and the large density of FeSi layer derived from XRR fitting results in FeSi(001)/Pt(001) sample. The first one may degrade the transmission efficiency of spin current across the interface and be responsible for the large increase of Δa comparing with the relative small increase of Δa Δa in FeSi(001)/Pt(111) sample [28], while the last one may lead to the invalidity of the reference for the FeSi(001)/AlO$_x$ control sample. Thus, the Pt thickness dependence of damping constant in FeSi(001)/Pt(001) sample does not further proceed. Furthermore, to test the reproducibility of the crystallographic direction dependence of the increase in damping constant for FeSi(001)/Pt(111) samples compared with the reference sample, and to get the spin-mixing conductance between FeSi and Pt, a series of FeSi(001)/Pt(111) sample was fabricated with only varying the thickness of Pt. Then, the frequency-dependent FMR measurements were carried out. Figures 6(a) and 6(b) show the resonance field H_r along the easy axis and hard axis of FeSi for FeSi(001)/Pt(111) samples. One can see that H_r slightly decreases when the Pt(111) layer is deposited and then is almost independent of the t_{Pt} at different resonance frequencies. It suggests that a small extra interfacial magnetic anisotropy is induced in FeSi layer once the Pt layer is deposited above the FeSi layers. From the frequency-dependent linewidth, the damping constants can be obtained according

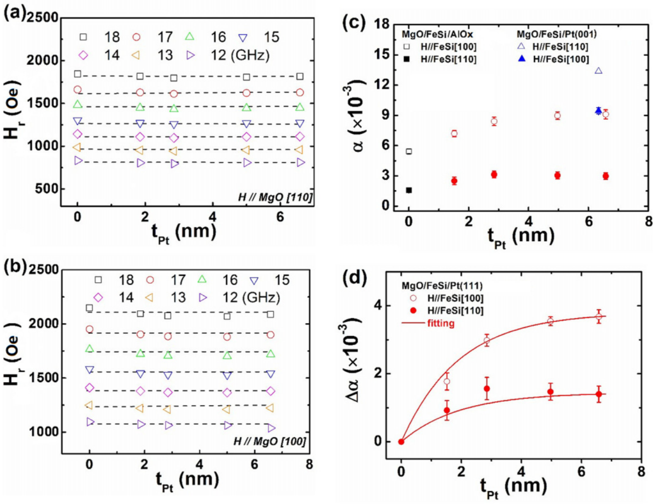

FIG. 6. Pt thickness-dependent resonance field H_r at various frequencies for FeSi/Pt(111) along easy (a) or hard axis (b) of FeSi, damping constant α (c), and the Δa for all samples (d).

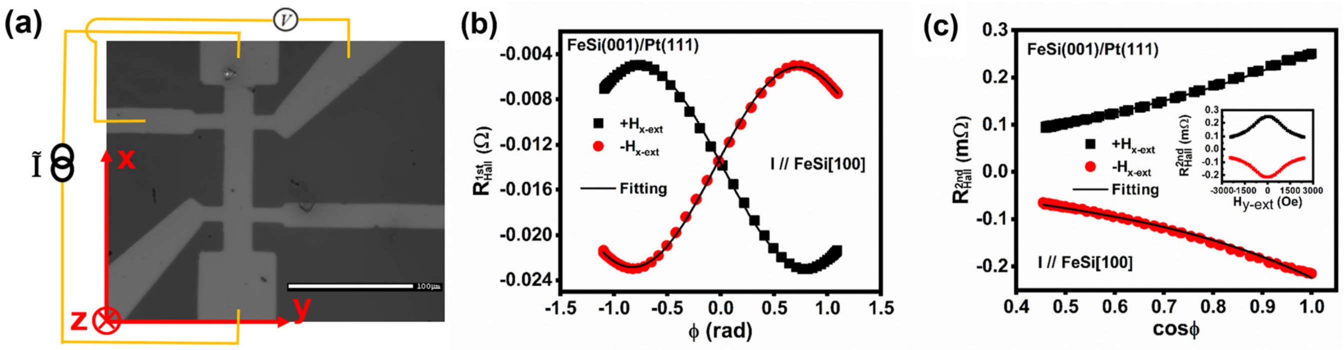

FIG. 7. The optical graph of the patterned Hall bar with measurement configurations (a), an exemplary first- (b) and second- (c) order harmonic Hall resistance vs angle ϕ and cosϕ with fixed external field $H_{x\text{-ext}} = 1245$ Oe along $\pm x$ axis. The external field $H_{y\text{-ext}}$ is swept from -2500 to 2500 Oe and the magnitude of alternative current density $J_e = 9.6\,\text{MA/cm}^2$ along the [100] direction of FeSi (easy axis). The fitting curves are based on Eq. (4). The scale bar in (a) is 100 μm. The inset in (c) shows the second-order Hall resistance vs $H_{y\text{-ext}}$.

to Eq. (2), and the results are shown in Fig. 6(c). It can be seen that the damping constant is different with the applied field along EA and HA of FeSi(001) in FeSi(001)/Pt(111) samples. The spin-pumping induced extra damping Δa was also determined as shown in Fig. 6(d). The results confirm the reproducibility of the crystallographic direction-dependent increase in damping constant for FeSi(001)/Pt(111) samples. It should be mentioned that the large difference of Δa in FeSi(001)/Pt(111) sample comparing with the reference sample may not be ascribed to the contribution from TMS of FeSi due to the Pt coverage, because Δa along EA and HA are estimated by subtracting the corresponding values from the reference FeSi(001)/AlO$_x$ sample. In addition, Zhu *et al.* reported that TMS-induced damping decays to a quite small value when the FM thickness is in the large region for the FM-thickness dependence of α in the in-plane magnetized HM/FM systems [28]. So, our results shown in Fig. 6 indicate that the extrinsic contribution-induced increase in α due to TMS is negligibly small [36,45]. Thus, the difference of Δa along EA and HA could be ascribed to the anisotropic absorption of spin current in epitaxial Pt(111) layer. The increase in Δa either along EA or HA with the increasing t_{Pt} can be ascribed to the gradual decrease in spin current back-flow effect when t_{Pt} is larger than its spin diffusion length λ_{SD} [46]. Considering the spin current back-flow effect, spin-pumping induced extra damping can be expressed as [46–50]

$$\Delta\alpha = \alpha - \alpha_0 = g\mu_{\text{B}} \frac{g_{\text{eff}}^{\uparrow\downarrow}}{4\pi M_{\text{S}}} \frac{1}{t_{\text{FeSi}}} (1 - e^{(-2t_{\text{Pt}})/\lambda_{\text{SD}}}), \tag{3}$$

where α_0 stands for the damping constant of the reference sample, $g^{\uparrow\downarrow}$ is the spin-mixing conductance of the whole sample. The data fitting for FeSi(001)/Pt(111) sample in Fig. 6(c) based on Eq. (3) gives the spin-mixing conductance around $2.86 \times 10^{19}\,\text{m}^{-2}$ and $1.72 \times 10^{19}\,\text{m}^{-2}$, while λ_{SD} is around 4.52 and 2.49 nm along EA and HA, respectively. The obtained values are compatible with the previous studies in a polycrystalline Pt-covered FM film [9,51]. The observed anisotropic incremental damping constant, spin-mixing conductance, and spin-diffusion length along different crystallographic directions of Pt may reflect a large angular dependence of spin-orbit coupling near the interface of the epitaxial FeSi/Pt bilayer contributed by spin-orbit potential and exchange splitting as predicted in a theoretical work [52].

To further confirm the crystallographic direction-dependent spin Hall effect in epitaxial Pt(111), the FeSi(001)/Pt(111) samples with $t_{\text{Pt}} = 7\,\text{nm}$ was patterned to Hall bars with current channel either parallel to the EA or HA of FeSi. Then, the dampinglike and fieldlike spin-orbit torques were measured by a harmonic Hall voltage measurements method [14]. In this method, both an alternative current and a constant bias field $H_{x\text{-ext}}$ are applied along the current channel of Hall bars. Meanwhile, a magnetic field $H_{y\text{-ext}}$ is swept in the orthogonal directions respect to the current channel. The generated first and second harmonic Hall resistance can be expressed as [14]

$$R_{\text{Hall}}^{\text{1st}} = R_{\text{PHE}} \sin 2\phi;$$
$$R_{\text{Hall}}^{\text{2nd}} = \frac{H_{\text{DL}} R_{\text{AHE}}}{2H_{\text{sat}}} X + \frac{H_{\text{FL}} R_{\text{PHE}}}{H_{x-\text{ext}}} (2X^4 - X^2). \tag{4}$$

where R_{PHE} is the planar Hall resistance, R_{AHE} is the anomalous Hall resistance, H_{sat} is the out-of-plane saturation field, and $X = \cos\phi$ with ϕ the angle between current channel and the direction of the in-plane projected magnetization. Here $\phi \approx \arctan(H_{y\text{-ext}}/H_{x\text{-ext}})$. H_{D} and H_{FL} represent the dampinglike and fieldlike SOT fields, respectively.

Figure 7 shows the exemplary first and second-order harmonic Hall resistances vs azimuthal angle ϕ for FeSi(001)/Pt(111) sample with current channel parallel to the easy axis of FeSi. The external field $H_{x\text{-ext}}$ is fixed as 1245 Oe along the $\pm x$ axis (namely the easy axis of FeSi here) and the alternative current density J_{e} is $9.6\,\text{MA/cm}^2$ along the $\pm x$ axis. The out-of-plane saturation field H_{sat} and the anomalous Hall resistance R_{AHE} are, respectively, around 20 135.5 Oe and 0.25 Ω for FeSi(001)/Pt(111) sample by measuring the Hall resistance with the magnetic field applied along the out-of-plane direction. Then, the effective SOT fields H_{DL}, H_{FL} can be obtained by fitting the data with Eq. (4). Through changing the current density, a bunch of the second-order harmonic Hall resistance curves can be obtained as shown in Figs. 8(a) and 8(b). Figures 8(c) and 8(d) show the obtained $H_{\text{DL(FL)}}$ with the variation of J_{e} with quite linear dependence. The dampinglike and fieldlike torque efficiency

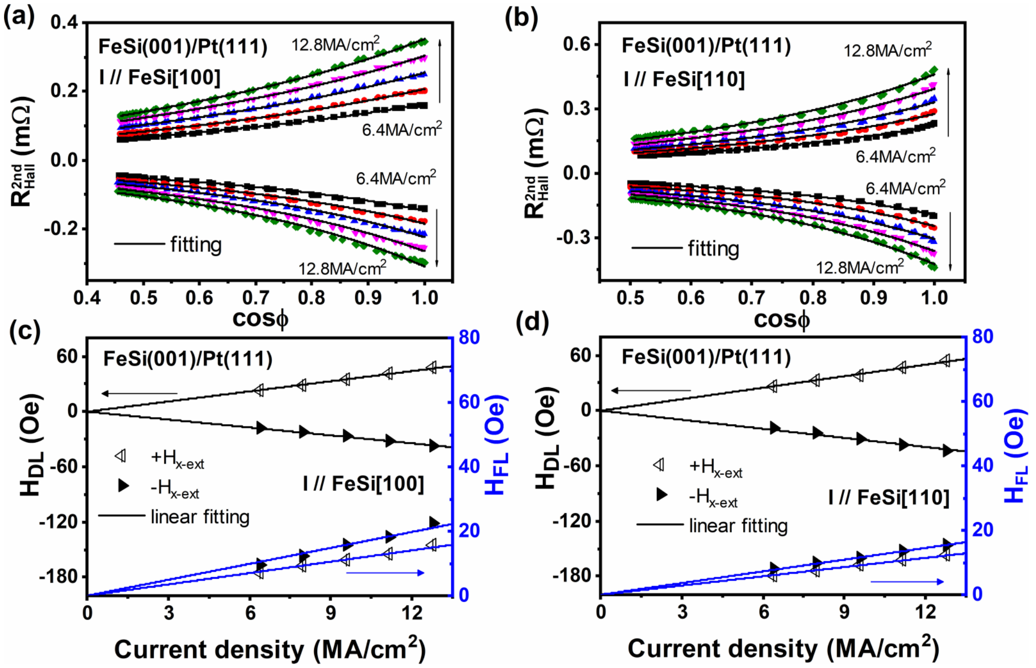

FIG. 8. The second-order harmonic Hall resistance vs cosϕ with the variation of magnitude of the alternative current density from 6.4–12.8 MA/cm^2 for FeSi(001)/Pt(111) and current direction along FeSi[100] (a) and FeSi[110] (b), the dampinglike and fieldlike fields vs current density with current direction along FeSi[100] (c) and FeSi[110] (d).

$\beta_{\mathrm{DL(FL)}}$ is defined by $\beta_{\mathrm{DL(FL)}} = H_{\mathrm{DL(FL)}}/J_e$. So, the linear fitting of $H_{\mathrm{DL(FL)}}$ vs J_e gives β_{DL} around 3.28 ± 0.03 and $3.72 \pm 0.06\,\mathrm{Oe/MA\ cm^2}$ when the current is applied along EA and HA of FeSi(001) films, respectively, while β_{FL} is around 1.41 ± 0.03 and $1.08 \pm 0.01\ \mathrm{Oe/MA\ cm^2}$ when the current is applied along EA and HA of FeSi(001) films, respectively. The obtained spin-orbit torque efficiency of Pt is on the same order with our previous reports in Pt/Co/AlO$_x$ sample [53]. The large difference of spin-orbit torque efficiency $\beta_{\mathrm{DL(FL)}}$ indicates the different conversion abilities from electric current to spin current and the anisotropic spin Hall effect in epitaxial Pt(111) [54]. In epitaxial Pt, the intrinsic Berry curvature mechanism may show the dominant contribution to the spin Hall effect rather than the extrinsic spin side jump and skew-scattering mechanism [55]. The Berry curvature of Pt changes sharply at some high symmetrical points in wave-vector space, which may contribute the anisotropic spin Hall effect in epitaxial Pt. This anisotropic spin Hall effect from harmonic Hall voltage measurement has further confirmed the above-proposed anisotropic spin-orbit coupling in epitaxial Pt by FMR measurement. However, there is a contradictory observation with that the higher the dampinglike spin-orbit torque efficiency, the smaller the extra increase in damping constant in FeSi(001)/Pt(111) sample. The contradictory result was also reported in Co/Hf/Pt trilayers, in which the trend of the larger the dampinglike SOT efficiency, the smaller the damping constant was reported [28]. They found that the interfacial spin-orbit coupling could significantly decrease the spin-orbit torque efficiency exerted on the FM layer via degradation of the spin current transparency for the interface. Thus, the interfacial spin-orbit coupling could also induce strong spin memory loss, which gives a relative high damping constant in spin-pumping process. It reveals that the interfacial spin-orbit coupling leads to the decrease of spin current transparency and the increase of spin memory loss, and plays an important role in the spin current transmission process. In our sample, although the interface roughness in FeSi(001)/Pt(111) bilayers is only around 0.36 nm as shown in Fig. 2, the interfacial spin-orbit coupling may still have large influence on the spin current transmission process. However, the explanation about Co/Hf/Pt trilayers does not apply to our case since the interface is the same for two crystallographic directions in FeSi(001)/Pt(111) sample. Recently, the anisotropic spin current absorption phenomenon was observed in NiFe/Cr/CoFe spin valves with the single-crystalline CoFe layer as the spin current absorption layer and the polycrystalline NiFe as spin current generation layer [39]. It may suggest that the epitaxial FeSi also shows crystallographic direction-dependent spin current generation/absorption properties. Thus, the generation of spin current from epitaxial Pt(111) is anisotropic and the absorption of the spin current by epitaxial FeSi may also be anisotropic in the harmonic Hall voltage measurement. However, only anisotropic spin current absorption in Pt(111) is involved in the FMR measurement since the crystallographic direction-dependent spin current generation was subtracted from the FeSi(001)/AlO$_x$ reference sample. The different spin current generation/absorption in epitaxial FeSi and Pt may result in the contradictory between the spin-pumping and spin-orbit torque experimental results.

IV. CONCLUSIONS

In summary, by choosing the small lattice mismatch materials with MgO(001) single-crystal substrates, we have systematically investigated the spin dynamic and transport properties in Fe$_{0.79}$Si$_{0.21}$(001)/Pt(111) samples. XRD patterns, TEM image, and the static magnetic properties measurement indicate a high-quality epitaxial structure of FeSi and Pt layer with fourfold magnetocrystalline anisotropy of FeSi films. The damping constant is around 0.0054 and 0.0016 for the reference $\mathrm{Fe}_{0.79}\mathrm{Si}_{0.21}(001)/\mathrm{AlO}_x$ sample with analyzing the dynamic magnetic properties using FMR with the magnetic field along the easy and hard axes of $\mathrm{Fe}_{0.79}\mathrm{Si}_{0.21}$, respectively. Compared with the reference sample, the additional damping constant is 3.68×10^{-3} and 1.40×10^{-3} for $\mathrm{Fe}_{0.79}\mathrm{Si}_{0.21}(001)/\mathrm{Pt}(111)$ sample with $t_{\mathrm{Pt}} = 7\,\mathrm{nm}$ and the magnetic field along easy and hard axes of $\mathrm{Fe}_{0.79}\mathrm{Si}_{0.21}$, respectively. Our results indicate that the different crystallographic directions of Pt give rise to the different damping constants, which may be ascribed to the different spin current absorption efficiencies in epitaxial Pt due to the anisotropic spin Hall effect in Pt(111) layer. The Pt thickness-dependent additional increment of damping constant gives an anisotropic spin-mixing conductance in epitaxial Pt layer. The harmonic Hall voltage measurement also illustrates anisotropic spin-orbit torque efficiency along different axes in $\mathrm{Fe}_{0.79}\mathrm{Si}_{0.21}(001)/\mathrm{Pt}(111)$. The quite large difference of spin-mixing conductance and SOT efficiency between EA and HA in FeSi(001)/Pt(111) sample may suggest an anisotropic spin Hall effect in epitaxial Pt layer and the crystallographic direction related spin current transmission process.

ACKNOWLEDGMENTS

We thank Prof. Junwei Zhang and Prof. Y. Peng at Electron Microscopy Centre of Lanzhou University for their assistance to obtain the TEM images. This work was supported by the National Natural Science Foundation of China (Grants No. 91963201 and No. 51671098), PCSIRT (Grant No. IRT16R35), the 111 Project (Grant No. B20063), and the Natural Science Foundation of Gansu Province (Grant No. 17JR5RA210).

---

[1] K. S. Ryu, L. Thomas, S. H. Yang, and S. Parkin, Nat. Nanotechnol. **8**, 527 (2013).

[2] K. Garello, F. Yasin, H. Hody, S. Couet, L. Souriau, S. H. Sharifi, J. Swerts, R. Carpenter, S. Rao, W. Kim, J. Wu, K. K. V. Sethu, M. Pak, N. Jossart, D. Crotti, A. Furnemont, and G. S. Kar, *2019 Symposium on VLSI Circuits T194* (IEEE, 2019).

[3] K. Gilmore, Y. U. Idzerda, and M. D. Stiles, Phys. Rev. Lett. **99**, 027204 (2007).

[4] B. Heinrich, C. Burrowes, E. Montoya, B. Kardasz, E. Girt, Y. Y. Song, Y. Y. Sun, and M. Z. Wu, Phys. Rev. Lett. **107**, 066604 (2011).

[5] S. Bhatti, R. Sbiaa, A. Hirohata, H. Ohno, S. Fukami, and S. N. Piramanayagam, Mater. Today **20**, 530 (2017).

[6] Y. Tserkovnyak, A. Brataas, and G. E. W. Bauer, Phys. Rev. Lett. **88**, 117601 (2002).

[7] Y. Tserkovnyak, A. Brataas, and G. E. W. Bauer, Phys. Rev. B **66**, 224403 (2002).

[8] T. L. Gilbert, IEEE Trans. Magn. **40**, 3443 (2004).

[9] M. Tokac, S. A. Bunyaev, G. N. Kakazei, D. S. Schmool, D. Atkinson, and A. T. Hindmarch, Phys. Rev. Lett. **115**, 056601 (2015).

[10] A. Wittmann, G. Schweicher, K. Broch, J. Novak, V. Lami, D. Cornil, E. R. McNellis, O. Zadvorna, D. Venkateshvaran, K. Takimiya, Y. H. Geerts, J. Cornil, Y. Vaynzof, J. Sinova, S. Watanabe, and H. Sirringhaus, Phys. Rev. Lett. **124**, 027204 (2020).

[11] L. Q. Liu, O. J. Lee, T. J. Gudmundsen, D. C. Ralph, and R. A. Buhrman, Phys. Rev. Lett. **109**, 096602 (2012).

[12] I. M. Miron, K. Garello, G. Gaudin, P. J. Zermatten, M. V. Costache, S. Auffret, S. Bandiera, B. Rodmacq, A. Schuhl, and P. Gambardella, Nature (London) **476**, 189 (2011).

[13] J. Kim, J. Sinha, M. Hayashi, M. Yamanouchi, S. Fukami, T. Suzuki, S. Mitani, and H. Ohno, Nat. Mater. **12**, 240 (2013).

[14] F. L. Luo, S. Goolaup, W. C. Law, S. H. Li, F. N. Tan, C. Engel, T. J. Zhou, and W. S. Lew, Phys. Rev. B **95**, 174415 (2017).

[15] O. Mosendz, J. E. Pearson, F. Y. Fradin, G. E. W. Bauer, S. D. Bader, and A. Hoffmann, Phys. Rev. Lett. **104**, 046601 (2010).

[16] A. B. Cahaya, A. O. Leon, and G. E. W. Bauer, Phys. Rev. B **96**, 144434 (2017).

[17] M. Isasa, A. Bedoya-Pinto, S. Velez, F. Golmar, F. Sanchez, L. E. Hueso, J. Fontcuberta, and F. Casanova, Appl. Phys. Lett. **105**, 142402 (2014).

[18] T. Qu, and R. H. Victora, Phys. Rev. B **93**, 224426 (2016).

[19] W. Zhang, M. B. Jungfleisch, F. Freimuth, W. J. Jiang, J. Sklenar, J. E. Pearson, J. B. Ketterson, Y. Mokrousov, and A. Hoffmann, Phys. Rev. B **92**, 144405 (2015).

[20] K. Ando, S. Takahashi, J. Ieda, Y. Kajiwara, H. Nakayama, T. Yoshino, K. Harii, Y. Fujikawa, M. Matsuo, S. Maekawa, and E. Saitoh, J. Appl. Phys. **109**, 103913 (2011).

[21] A. Azevedo, L. H. Vilela-Leão, R. L. Rodriguez-Suárez, A. F. Lacerda Santos, and S. M. Rezende, Phys. Rev. B **83**, 144402 (2011).

[22] Z. Feng, J. Hu, L. Sun, B. You, D. Wu, J. Du, W. Zhang, A. Hu, Y. Yang, D. M. Tang, B. S. Zhang, and H. F. Ding, Phys. Rev. B **85**, 214423 (2012).

[23] L. Q. Liu, T. Moriyama, D. C. Ralph, and R. A. Buhrman, Phys. Rev. Lett. **106**, 036601 (2011).

[24] O. Mosendz, V. Vlaminck, J. E. Pearson, F. Y. Fradin, G. E. W. Bauer, S. D. Bader, and A. Hoffmann, Phys. Rev. B **82**, 214403 (2010).

[25] X. B. Guo, X. M. Han, Y. L. Zuo, J. W. Zhang, D. Li, B. S. Cui, K. Wu, J. J. Yun, T. Wang, Y. Peng, and L. Xi, Appl. Phys. Lett. **108**, 152401 (2016).

[26] X. B. Guo, K. Wu, B. S. Cui, D. Li, J. J. Yun, Y. L. Zuo, H. P. Zuo, T. Wang, and L. Xi, J. Phys. D: Appl. Phys. **49**, 055005 (2016).

[27] H. L. Wang, C. H. Du, Y. Pu, R. Adur, P. C. Hammel, and F. Y. Yang, Phys. Rev. Lett. **112**, 197201 (2014).

[28] L. J. Zhu, D. C. Ralph, and R. A. Buhrman, Phys. Rev. Lett. **122**, 077201 (2019).

[29] M. Bjorck, and G. Andersson, J. Appl. Crystallogr. **40**, 1174 (2007).

[30] J. J. Yun, Y. L. Zuo, J. Mao, M. X. Chang, S. X. Zhang, J. Liu, and L. Xi, Appl. Phys. Lett. **115**, 032404 (2019).

[31] Y. L. Yin, F. Pan, M. Ahlberg, M. Ranjbar, P. Durrenfeld, A. Houshang, M. Haidar, L. Bergqvist, Y. Zhai, R. K. Dumas, A. Delin, and J. Akerman, Phys. Rev. B **92**, 024427 (2015).

[32] K. H. Ahn, S. Baik, and S. S. Kim, J. Mater. Res. **17**, 2334 (2002).

[33] B. Heinrich, J. F. Cochran, M. Kowalewski, J. Kirschner, Z. Celinski, A. S. Arrott, and K. Myrtle, Phys. Rev. B **44**, 9348 (1991).

[34] L. H. Bai, Y. S. Gui, A. Wirthmann, E. Recksiedler, N. Mecking, C. M. Hu, Z. H. Chen, and S. C. Shen, Appl. Phys. Lett. **92**, 032504 (2008).

[35] A. Conca, S. Keller, M. R. Schweizer, E. T. Papaioannou, and B. Hillebrands, Phys. Rev. B **98**, 214439 (2018).

[36] S. Husain, A. Kumar, V. Barwal, N. Behera, S. Akansel, P. Svedlindh, and S. Chaudhary, Phys. Rev. B **97**, 064420 (2018).

[37] M. Belmeguenai, H. Tuzcuoglu, M. S. Gabor, T. Petrisor, C. Tiusan, D. Berling, F. Zighem, T. Chauveau, S. M. Cherif, and P. Moch, Phys. Rev. B **87**, 184431 (2013).

[38] K. Zakeri, J. Lindner, I. Barsukov, R. Meckenstock, M. Farle, U. von Horsten, H. Wende, W. Keune, J. Rocker, S. S. Kalarickal, K. Lenz, W. Kuch, K. Baberschke, and Z. Frait, Phys. Rev. B **76**, 104416 (2007).

[39] A. A. Baker, A. I. Figueroa, C. J. Love, S. A. Cavill, T. Hesjedal, and G. van der Laan, Phys. Rev. Lett. **116**, 047201 (2016).

[40] K. Lenz, H. Wende, W. Kuch, K. Baberschke, K. Nagy, and A. Janossy, Phys. Rev. B **73**, 144424 (2006).

[41] X. Ma, G. Q. Yu, X. Li, T. Wang, D. Wu, K. S. Olsson, Z. D. Chu, K. M. An, J. Q. Xiao, K. L. Wang, and X. Q. Li, Phys. Rev. B **94**, 180408(R) (2016).

[42] Y. Li, F. L. Zeng, S. S.-L. Zhang, H. Shin, H. Saglam, V. Karakas, O. Ozatay, J. E. Pearson, O. G. Heinonen, Y. Wu, A. Hoffmann, and W. Zhang, Phys. Rev. Lett. **122**, 117203 (2019).

[43] R. Yilgin, Y. Sakuraba, M. Oogane, S. Mizukami, Y. Ando, and T. Miyazaki, Jpn. J. Appl. Phys. **246**, L205 (2007).

[44] F. L. Zeng, X. Shen, Y. Li, Z. Yuan, W. Zhang, and Y. Z. Wu, New J. Phys. **22**, 093047 (2020).

[45] N. Behera, A. Kumar, S. Chaudhary, and D. K. Pandya, RSC Adv. **7**, 8106 (2017).

[46] J. M. Shaw, H. T. Nembach, and T. J. Silva, Phys. Rev. B **85**, 054412 (2012).

[47] M. Farle, Rep. Prog. Phys. **61**, 755 (1998).

[48] Y. Tserkovnyak, A. Brataas, G. E. W. Bauer, and B. I. Halperin, Rev. Mod. Phys. **77**, 1375 (2005).

[49] S. Azzawi, A. Ganguly, M. Tokac, R. M. Rowan-Robinson, J. Sinha, A. T. Hindmarch, A. Barman, and D. Atkinson, Phys. Rev. B **93**, 054402 (2016).

[50] Y. Li, S. J. Yang, D. L. Sun, Y. B. Sun, Y. Li, E. Vetter, R. Sun, N. Li, X. Yang, L. Su, Z. Z. Gong, Z. K. Xie, J. J. Zhao, W. He, X. Q. Zhang, and Z. H. Cheng, Phys. Rev. B **102**, 014420 (2020).

[51] M. Obstbaum, M. Hartinger, H. G. Bauer, T. Meier, F. Swientek, C. H. Back, and G. Woltersdorf, Phys. Rev. B **89**, 060407(R) (2014).

[52] K. S. Lee, D. Go, A. Manchon, P. M. Haney, M. D. Stiles, H. W. Lee, and K. J. Lee, Phys. Rev. B **91**, 144401 (2015).

[53] D. Li, S. W. Chen, Y. J. Zuo, J. J. Yun, B. S. Cui, K. Wu, X. B. Guo, D. Z. Yang, J. B. Wang, and L. Xi, Sci. Rep.-Uk **8**, 12959 (2018).

[54] Q. Bai, J. Mao, J. Yun, Y. Zhai, M. Chang, X. Zhang, J. Zhang, Y. Zuo, and L. Xi, Appl. Phys. Lett. **118**, 132403 (2021).

[55] A. Hoffmann, IEEE Trans. Magn. **49**, 5172 (2013).